

Soft X-ray Transmission Spectroscopy of Warm/Hot Intergalactic Medium: Mock Observation of Gamma-Ray Burst X-ray Afterglow

Hajime KAWAHARA¹, Kohji YOSHIKAWA¹, Shin SASAKI² Yasushi SUTO¹, Nobuyuki KAWAI³, Kazuhisa MITSUDA⁴, Takaya OHASHI², and Noriko Y. YAMASAKI⁴

¹*Department of Physics, School of Science, The University of Tokyo, Tokyo 113-0033*

kawahara@utap.phys.s.u-tokyo.ac.jp

²*Department of Physics, Tokyo Metropolitan University,
1-1 Minami-Osawa, Hachioji, Tokyo 192-0397*

³*Department of Physics, Tokyo Institute of Technology,
2-12-1 Ookayama, Meguro-ku, Tokyo 152-8551*

⁴*The Institute of Space and Astronautical Science (ISAS),
Japan Aerospace Exploration Agency (JAXA),
3-1-1 Yoshinodai, Sagami-hara, Kanagawa 229-8510*

(Received 2005 April 27; accepted 2005)

Abstract

We discuss the detectability of Warm/Hot Intergalactic medium (WHIM) via the absorption lines toward bright gamma-ray burst (GRB) afterglows with future X-ray satellite missions like *XEUS*. We create mock absorption spectra for bright GRB afterglows (~ 40 per year over the entire sky) using a light-cone output of a cosmological hydrodynamic simulation. We assume that WHIM is under collisional and photo-ionization equilibrium. If we adopt the constant metallicity of $Z = 0.1Z_{\odot}$, approximately one OVII absorption line system with $> 3\sigma$ will be detected on average along a random line-of-sight up to $z = 0.3$ if *XEUS* starts observing within a couple of hours after the GRB alert. However the above number is very sensitive to the adopted, and currently unknown, metallicity of the WHIM. We also discuss a feasibility of a follow-up observation for the emission line counterpart with a small dedicated X-ray mission like *DIOS* (Diffuse Intergalactic Oxygen Surveyor) and reliability of the estimate of the cosmic baryon density.

Key words: cosmology: miscellaneous — X-rays: general — methods: numerical

1. Introduction

More than 50 percent of cosmic baryons is dark (000 [cite]cite.Fukugita1998Fukugita, Hogan, & Peebles(1998); 000 [cite]cite.Fukugita2004Fukugita & Peebles(2004)). The abundance, physical properties, and spatial distribution of such dark baryons constitute one of the most important unsolved problems in observational cosmology. Recent numerical simulations suggest that a major fraction of dark baryons is in the form of WHIM (Warm/Hot Intergalactic medium) roughly with temperature $10^5\text{K} < T < 10^7\text{K}$ and over-density $1 < \delta < 1000$ (000 [cite]cite.Cen1999aCen & Ostriker(1999a); 000 [cite]cite.Dave2001Davé et al.(2001)). WHIM traces the large-scale filamentary structure of mass (dark matter) distribution more faithfully than hot intracluster gas ($T > 10^7\text{K}$ typically) and galaxies both of which preferentially reside in clusters that form around the knot-like intersections of the filamentary regions (e.g., Suto et al. 2004a, 2004b; Kang et al. 2005). This implies that WHIM carries important cosmological information in a complementary fashion to distributions of galaxies in optical and of clusters in X-ray.

DIOS (Diffuse Intergalactic Oxygen Surveyor) is a dedicated soft X-ray mission which aims at unveiling dark baryons in the universe (000 [cite]cite.Ohashi2003Ohashi et al.(2003)) via oxygen emission from WHIM. Detectability of such emission features was examined in detail both for mock blank survey (000 [cite]cite.Yoshikawa2003Yoshikawa et al.(2003); hereafter Paper I) and for mock targeted survey of outskirts of clusters in the local universe (000 [cite]cite.Yoshikawa2004Yoshikawa et al.(2004); hereafter Paper II). These authors find that approximately 20 percent of cosmic baryons leaves emission signatures detectable by *DIOS*. This fraction corresponds to a relatively higher temperature tail of the entire WHIM distribution, i.e., $10^6\text{K} < T < 10^7\text{K}$ is sensitive to the assumed metallicity of WHIM. They adopt a metallicity model proposed by te]cite.Cen1999bCen & Ostriker(1999b) ([cite]cite.Cen1999bCen & Ostriker(1999b)) and te]cite.Aguirre2001Aguirre et al.(2001) ([cite]cite.Aguirre2001Aguirre et al.(2001)), but the metallicity of WHIM is admittedly very uncertain at this moment.

Another complementary strategy of detecting elusive WHIM is to search for its absorption signatures. In fact, several independent groups reported successful detections of absorption lines of highly ionized metals in spectra of background QSOs and clusters; OVII and OVIII by te]cite.Fang2002aFang, Bryan, Canizares(2002) ([cite]cite.Fang2002aFang, Bryan, Canizares(2002)), OVI at $z \sim 0.2$ in the *FUSE* spectrum of QSO H1821+643 by te]cite.Tripp2000Tripp, Savage & Jenkins(2000) ([cite]cite.Tripp2000Tripp, Savage & Jenkins(2000)), and more recently O VII, N VII and NVI along the line of sight to the Blazar Mkn 421 by te]cite.Nicastro2005Nicastro et al.(2005) ([cite]cite.Nicastro2005Nicastro et al.(2005)); see also 000 [cite]cite.Nicastro2002Nicastro et al.(2002); 000 [cite]cite.Fang2002bFang et al.(2002); 000 [cite]cite.Mathur2003Mathur et al.(2003); 000 [cite]cite.Fujimoto2004Fujimoto et al.(2004).

In particular [Nicastro et al. \(2005\)](#) ([Nicastro et al. \(2005\)](#)) estimate $\Omega_b^{\text{WHIM}} = (2.7_{-1.9}^{+3.8}\%) \times 10^{-[\text{O}/\text{H}]-1}$ adopting a temperature of $10^{6.1}\text{K}$ for the WHIM, where $10^{[\text{O}/\text{H}]-1}$ is the oxygen-to-hydrogen number density ratio in units of 0.1 times the solar value. While the above value seems to be in good agreement with that expected from the previous simulations ([Cen & Ostriker \(1999a\)](#); [Davé et al. \(2001\)](#)), the estimate is still sensitive to the assumed temperature and metallicity of the WHIM along the single line of sight to Mkn 421.

This paper examines the detectability of WHIM via absorption, instead of emission, lines using the same cosmological hydrodynamic simulation data as Paper I. In particular we consider gamma-ray burst (GRB) X-ray afterglows as a bright X-ray lighthouse, and create mock absorption spectra for future X-ray missions such as *XEUS* (X-ray Evolving-Universe Spectroscopy). The idea of probing WHIM using with GRB afterglow was first proposed by [Fiore et al. \(2000\)](#) ([Fiore et al. \(2000\)](#)). This paper extends their analysis and examines the detectability much in detail using a realistic numerical simulation output. The same methodology can be applied to any bright QSOs in principle; Mkn 421 is one of the most promising targets as already demonstrated successfully by [Nicastro et al. \(2005\)](#) ([Nicastro et al. \(2005\)](#)).

In addition to its intrinsic brightness, the more important advantage of GRB for the WHIM science lies in its temporal behavior; once absorption lines due to WHIM are detected, one can perform deep follow-up observations to look for the emission counterpart (Papers I and II) after the GRB is completely faded. Such follow-ups can be done either with the same X-ray telescope or with a small dedicated mission like *DIOS*. In reality, we hope that *DIOS* will be launched much earlier than *XEUS*, but we still refer to its future successor in this context as *DIOS* for simplicity. Successful detections of both absorption and emission features will offer unambiguous evidence of WHIM.

The rest of the paper is organized as follows; §2 describes our methodology and model assumptions in computing mock transmission spectra of the GRB afterglow through WHIM. We present examples of mock spectra and their basic statistics in §3. We discuss the detectability of WHIM via absorption in §4 and also consider how to extract physical properties of WHIM by combining its emission features detectable by *DIOS*. Finally §5 is devoted to the conclusions of the paper and to further discussion.

2. Creating Mock Transmission Spectra of WHIM through GRB afterglow from Cosmological Hydrodynamic Simulations

We compute mock transmission spectra of WHIM using the same simulation data as Paper I. We create a stacked light-cone output for $0 < z < 0.3$ from the simulation data. Then we consider 6400 different line-of-sight directions, and compute mock spectra for a bright GRB afterglow taking into account the cosmic X-ray background (CXB) and UV background (UVB)

for photo-ionization sources. Our methodology is described in the following subsections.

2.1. Cosmological Hydrodynamic Simulation

We use the data of [Yoshikawa et al. \(2001\)](#) ([Yoshikawa et al. \(2001\)](#)) who performed a simulation with a hybrid code of Particle–Particle–Particle–Mesh (PPPM) Poisson solver and smoothed particle hydrodynamics (SPH). Both dark matter and gas employ 128^3 particles within a periodic simulation cube of $L_{\text{box}} = 75h^{-1}\text{Mpc}$ per side (in comoving). They adopt a standard ΛCDM model in which the density parameter $\Omega_{\text{m}} = 0.3$, the baryon density parameter $\Omega_b = 0.015h^{-2}$, the dimensionless cosmological constant $\Omega_{\Lambda} = 0.7$, the rms density fluctuation smoothed over a scale of $8h^{-1}\text{Mpc}$, $\sigma_8 = 1.0$, and the Hubble constant in units of 100km/s/Mpc $h = 0.7$. The simulation includes the effect of radiative cooling, but the energy feedback from supernova and the UV background heating are neglected. The adopted value of $\Omega_b = 0.03$ is $\sim 30\%$ smaller than the latest estimate by WMAP, $\Omega_b = (0.024 \pm 0.001)h^{-2}$ ([Spergel et al. \(2003\)](#)). In this sense our results may underestimate the real absorption and emission signatures by the corresponding amount.

We create a light-cone output for $0 < z < 0.3$ following [Yoshikawa et al. \(2003\)](#) ([Yoshikawa et al. \(2003\)](#)). The maximum value of $z = 0.3$ is adopted so as to ensure that the O VIII line is located in a spectrum region relatively free from the Galactic confusion (Paper I), while this may be very conservative. The output extends a $5^\circ \times 5^\circ$ region on the sky, which corresponds to the simulation boxsize at $z = 0.3$; $L_{\text{box}}/(1+0.3)/d_{\text{A}}(z=0.3) \approx 5^\circ$ with $d_{\text{A}}(z)$ being the angular diameter distance at redshift z .

2.2. Calculation of Optical Depths

Consider a line of sight (LOS) and denote its unit direction vector by $\hat{\mathbf{n}}$. We divide the LOS into 5000 separation bins x_i ($i = 1 \sim 5000$) so that their bin width is equal in comoving scale, i.e., $x_{i+1} - x_i = d_{\text{C}}(z=0.3)/5000$, where $d_{\text{C}}(z)$ is the comoving distance at redshift z . The gas density $\rho(x_i)$, temperature $T(x_i)$ and peculiar velocity $v_r(x_i)$ of the intergalactic medium (IGM) at the i -th bin are estimated by gathering contribution from all the simulation gas particles:

$$\rho(x_i) = \sum_{j=1}^N m W(x_i \hat{\mathbf{n}} - \mathbf{r}_j, h_j), \quad (1)$$

$$T(x_i) = \frac{1}{\rho(x_i)} \sum_{j=1}^N m T_j W(x_i \hat{\mathbf{n}} - \mathbf{r}_j, h_j), \quad (2)$$

$$v_r(x_i) = \frac{1}{\rho(x_i)} \sum_{j=1}^N m v_{r,j} W(x_i \hat{\mathbf{n}} - \mathbf{r}_j, h_j). \quad (3)$$

In the above expressions, j denotes an index for gas particles ($j = 1 \sim N$); T_j , $v_{r,j}$, \mathbf{r}_j , and h_j are temperature, peculiar velocity, position vector and smoothing length of the j -th gas par-

particle, and m is the mass of gas particles (independent of j). [cite]cite.Yoshikawa2001Yoshikawa et al.(2001) ([cite]cite.Yoshikawa2001Yoshikawa et al.(2001)) classify some fraction of gas particles as “galaxies” if they satisfy both the Jeans condition and the over-density criterion. Those particles are not included in the above summation. We adopt the smoothing kernel which is identical to that employed in the simulation (000 [cite]cite.Yoshikawa2001Yoshikawa et al.(2001)):

$$W(\mathbf{x} - \mathbf{r}, h) = \frac{1}{\pi h^3} \begin{cases} 1 - (3/2)u^2 + (3/4)u^3 & \text{if } 0 \leq u \leq 1 \\ (2 - u)^3/4 & \text{if } 1 \leq u \leq 2 \\ 0 & \text{otherwise} \end{cases}, \quad (4)$$

where $u \equiv |\mathbf{x} - \mathbf{r}|/h$.

We estimate the number density of an ionized metal A^{n+} (with charge $n+$) at the i -th bin as

$$n_{A^{n+}}(x_i) = \sum_{j=1}^N F_{A^{n+}}(T_j, \rho_j) \left(\frac{n_A}{n_H} \right)_j X m W(x_i \hat{\mathbf{n}} - \mathbf{r}_j, h_j), \quad (5)$$

where X is the hydrogen mass fraction (we adopt 0.755), m_A is the mass of the metal, and $Z_{A,j}$, $F_{A^{n+}}(T_j, \rho_j)$ and ρ_j represent the metallicity of A , the ionization fraction of A^{n+} , and density of the j -th gas particle. In most cases, we assume a constant metallicity for simplicity:

$$Z_{A,j} = 0.1 Z_{A,\odot}, \quad (6)$$

or equivalently a constant number ratio:

$$(n_A/n_H)_j = 0.1 (n_A/n_H)_\odot \quad (7)$$

independently of the time and the local density (see §3.1 below for other models).

Ionization fraction is calculated using a publicly available routine, SPEX ver. 1.10. Papers I and II assume collisional ionization equilibrium (CIE) for simplicity because detectable emission lines preferentially come from WHIM with relatively high density. In the absorption lines, however, lower-density WHIM may become important. So in this paper we take account of the photo-ionization effect and compute the ionization fraction of metals under the collisional and photo-ionization equilibrium (CPIE). In practice, we consider both CXB and UVB adopting the following fitting formulae (000 [cite]cite.Miyaji1998Miyaji et al.(1998); 000 [cite]cite.Shull1999Shull et al.(1999); 000 [cite]cite.Chen2003Chen et al.(2003)) for the differential energy distribution:

$$J_{\text{CXB}}(E) = J_1 \left(\frac{E}{\text{keV}} \right)^{-0.42}, \quad (8)$$

where $J_1 = 6.626 \times 10^{-26} \text{ erg cm}^{-2} \text{ s}^{-1} \text{ sr}^{-1} \text{ Hz}^{-1} (= 1.602 \times 10^{-8} \text{ erg cm}^{-2} \text{ s}^{-1} \text{ sr}^{-1} \text{ keV}^{-1})$, and

$$J_{\text{UV}}(E) = J_2 \left(\frac{E}{13.6 \text{ eV}} \right)^{-1.8}, \quad (9)$$

where $J_2 = 2.4 \times 10^{-23} \text{ erg cm}^{-2} \text{ s}^{-1} \text{ sr}^{-1} \text{ Hz}^{-1} (= 5.9 \times 10^{-6} \text{ erg cm}^{-2} \text{ s}^{-1} \text{ sr}^{-1} \text{ keV}^{-1})$. The resulting ionization fractions of OVII and OVIII for CIE and CPIE are plotted in Figure 1.

Finally we obtain the optical depth of the ionized metal A^{n+} along a LOS up to $z = 0.3$ as

$$\tau_{A^{n+}}(E) = \int_{z=0}^{z=0.3} n_{A^{n+}}(z) \sigma_{A^{n+}}(E') \frac{dl}{dz} dz, \quad (10)$$

where the rest-frame frequency E' is given by

$$E' = E(1+z)(1+v_r/c). \quad (11)$$

The absorption cross section $\sigma_{A^{n+}}(E')$ at E' is computed assuming the Doppler broadening:

$$\sigma_{A^{n+}}(E') = \sum_k \frac{\pi e^2}{m_e c} f_{k,A^{n+}} \frac{2\pi \hbar c}{\sqrt{\pi} E_k b_T} \exp \left[-\frac{c^2 (E' - E_k)^2}{b_T^2 E_k^2} \right], \quad (12)$$

where k denotes the index of different absorption lines of A^{n+} , $f_{k,A^{n+}}$ and E_k are the oscillator strength and the energy of the k -th line, and $b_T = (2k_B T/m_A)^{1/2}$ is the Doppler b -parameter (m_A is the mass of the metal A).

2.3. Mock Absorption Spectra of WHIM toward a bright GRB afterglow

Now we are in a position to compute mock absorption spectra of WHIM toward a bright GRB afterglow. Piro (2004) ([cite]cite.Piro2004Piro (2004)) pointed out that spectrum energy distribution of a typical GRB afterglow is approximated as

$$F_{\text{GRB}}(t, E) = F_0 \left(\frac{t}{40000\text{s}} \right)^{-\delta} \left(\frac{E}{1\text{keV}} \right)^{-\alpha}, \quad (13)$$

$$\delta = 1.2 \pm 0.2, \quad \alpha = 1.13 \pm 0.07. \quad (14)$$

For definiteness, we adopt the following :

$$F_{\text{GRB}}(t, E) = 6 \times 10^{-13} \left(\frac{t}{40000\text{s}} \right)^{-1.2} \left(\frac{E}{1\text{keV}} \right)^{-1.13} \text{ erg s}^{-1} \text{ cm}^{-2} \text{ keV}^{-1}. \quad (15)$$

For six years between 1997 and 2002, BeppoSax observed 8% of the entire sky (000 [cite]cite.Jager1997Jager et al 1997) and detected 10 GRB afterglows with $F_0 > 6 \times 10^{-13} \text{ erg s}^{-1} \text{ cm}^{-2} \text{ keV}^{-1}$. The brightest one has $F_0 = 6 \times 10^{-12} \text{ erg s}^{-1} \text{ cm}^{-2} \text{ keV}^{-1}$ (000 [cite]cite.Piro2004Piro (2004)). Assuming a nominal observational efficiency of 50%, GRB afterglows brighter than our fiducial value (Eq.[15]) are expected to be $\approx 10/0.5/0.08/6 = 42$ per year over the entire sky.

We consider mock observations of a GRB afterglow for $t_i < t < t_f$ after the GRB event ($t = 0$). Then the observed photon counts are computed by taking account of the absorption due to Galaxy and to the intervening WHIM:

$$\mathcal{N}(E) = \mathcal{N}_0(E) \exp \left[-\sum_{A^{n+}} \tau_{A^{n+}}(E) \right] \text{ [ph/eV]}, \quad (16)$$

$$\mathcal{N}_0(E) = S_{\text{eff}} \exp[-\sigma_{\text{gal}}(E) N_H] \int_{t_i}^{t_f} \frac{F_{\text{GRB}}(t, E)}{E} dt \text{ [ph/eV]}, \quad (17)$$

where $\mathcal{N}_0(E)$ determines the observable continuum level free from the WHIM absorption. The Galactic absorption is computed using the absorption cross section $\sigma_{gal}(E)$ in [cite.Morrison1983Morrison & McCammon(1983) ([cite]cite.Morrison1983Morrison & McCammon(1983)) who adopt 1 solar metallicity and the neutral hydrogen column density $N_H = 10^{20} \text{cm}^{-2}$. The Galactic extinction factor $\exp[-\sigma_{gal}(E)N_H]$ is ≈ 0.93 at $E = 0.6 \text{keV}$.

The detectability is very sensitive to the choice of t_i , which is determined by how rapidly *XEUS* can point to the target and start observation. If we assume $(t_i, t_f) = (1 \text{ hour}, 1 \text{ hour} + 5 \text{ ksec})$ and $(t_i, t_f) = (2 \text{ hour}, 2 \text{ hour} + 12 \text{ ksec})$, $\mathcal{N}_0(E = 500 \text{eV})$ reaches ~ 5000 [ph/eV] for *XEUS* (the effective area $S_{\text{eff}} = 60000 \text{cm}^2$ and the energy resolution $\Delta E = 2 \text{eV}$). In the case of the brightest GRB in the past ($F_0 = 6 \times 10^{-12} \text{ erg s}^{-1} \text{cm}^{-2} \text{keV}^{-1}$), an observation with $(t_i, t_f) = (1 \text{ day}, 1 \text{ day} + 15 \text{ ksec})$ can also have the similar number of \mathcal{N}_0 . For a longer exposure of $(t_i, t_f) = (1 \text{ day}, 1 \text{ day} + 30 \text{ ksec})$, \mathcal{N}_0 increases by a factor of 1.8. The choice of $t_i = 1$ day is more preferable for the TOO (time opportunity observation) mode since one can make a decision after other telescopes start observing and make sure that the flux of the GRB afterglow is indeed sufficient for the detection of WHIM absorption features. This number of photons determines the signal-to-noise ratio of our mock observation.

We adopt the energy range $300 \text{eV} < E < 1.5 \text{keV}$, because the line above 1.5 keV is not important for temperature of WHIM. Among hundreds of resonance absorption lines for $300 \text{eV} < E < 2 \text{keV}$ (000 [cite]cite.Verner1996Verner et al.(1996)), the most promising 10 absorption lines for detection (taking account of their abundance, the oscillator strength and the ionization fraction in the WHIM regime) are shown in Table 1.

2.4. Calculation of the Corresponding Emission Lines

If absorption line systems in the GRB afterglow are discovered, *DIOS* will carry out the follow-up survey of the same region in the sky later to search for the counterparts in emission lines. So we also compute the mock emission spectra (which are free from the GRB afterglow) for the same LOS in the simulated light-cone output. This can be done in a straight forward fashion following Paper I.

We divide the light-cone data into 80×80 square grids on the celestial plane (one grid size corresponds to 1 pixel size of *DIOS* $\approx 5^\circ/80 \approx 4'$) and 5000 equally-spaced (in comoving separation) bins along the LOS. Thus we have $80 \times 80 \times 5000$ cells in total (denoted by the index J). The surface brightness of a particular line $S_{J,l}$ of the J -th cell is

$$S_{J,l} = \sum_{i \in J} \frac{\rho_i m}{4\pi(1+z_i)^4 \Delta A_i} \left(\frac{X}{m_p} \right)^2 f_{e,i}^2 \epsilon_l(T_i, \rho_i, Z_i) [\text{erg s}^{-1} \text{cm}^{-2} \text{sr}^{-1}], \quad (18)$$

$$\Delta A_i = d_A^2(z_i) \Delta\omega, \quad (19)$$

where l is the index of the line, and the summation is over the gas particles (labeled i) within the J -th cell.

In the above expression, $\epsilon_l(T, \rho, Z)$ is the line emissivities ($[\text{erg s}^{-1} \text{cm}^3]$) normal-

ized to the electron densities as defined by [Mewe1985Mewe](#), [Gronenschild](#), & [van den Oord\(1985\)](#) ([Mewe1985Mewe](#), [Gronenschild](#), & [van den Oord\(1985\)](#)), $f_{e,i}$ is the electron number fraction of the i -th gas particle relative to the hydrogen and $\Delta\omega = (5^\circ/80)^2$ is the solid angle of the cell. The emissivities $\epsilon_l(T, \rho, Z)$ is calculated with SPEX ver. 1.10 under CPIPE adopting the same models for CXB and UVB discussed in §3.2.

Similarly we compute the energy spectrum of WHIM on a projected area of one pixel of *DIOS* along a particular LOS. The integrated flux between E and $E + \Delta E$ can be calculated by summing up over the gas particles in the cells along the LOS:

$$\mathcal{F}(E, E + \Delta E) = \sum_{i \in \text{LOS}} \frac{\rho_i m}{4\pi(1+z_i)^4 \Delta A_i} \left(\frac{X}{m_p}\right)^2 f_{e,i}^2 \times \int_{E(1+z_i)}^{(E+\Delta E)(1+z_i)} P(E', T_i, \rho_i, Z_i) dE' \quad [\text{erg s}^{-1} \text{cm}^{-2} \text{sr}^{-1}], \quad (20)$$

where $P(E, T, \rho, Z)$ is the template spectrum for temperature T , density ρ and metallicity Z . The set of template spectra $P(E, T, \rho, Z)$ is created with SPEX ver. 1.10 assuming CPIPE.

3. Results

3.1. Identification of absorption lines in mock spectra

Once mock spectra are constructed, our next task is to attempt the mock observation, in particular, to identify absorption lines in an objective manner. For this purpose, we follow the procedure described in [Fang2002aFang](#), [Bryan](#), [Canizares\(2002\)](#) ([Fang2002aFang](#), [Bryan](#), [Canizares\(2002\)](#)). Consider a schematic example of normalized absorption line profiles, $\exp(-\tau)$ as in Figure 2. We set a threshold value $F_{\text{th}} = 10^{-5}$, and identify a contiguous region below the threshold $1 - F_{\text{th}}$ as an absorption line system. If the line profile first down-crosses the $1 - F_{\text{th}}$ at $E = E_i$, and then up-crosses at $E = E_f$, the equivalent width W (in the observer's frame) of this system centered at $E = E_l$ is calculated by integrating $1 - \exp(-\tau)$ over $E_i < E < E_f$

$$W_l(E_l) = \int_{E_i}^{E_f} [1 - e^{-\tau(E)}] dE. \quad (21)$$

If the line system is identified as a particular species with the oscillator strength f_l , the equivalent width in its unsaturated regime is rewritten in terms of the corresponding column density N_l as:

$$N_l = \frac{9 \times 10^{14}}{f_l} \frac{W_l}{0.1 \text{eV}} \quad [\text{cm}^{-2}]. \quad (22)$$

In the present case, the S/N is determined by the energy resolution of the detector ($\Delta E = 2 \text{eV}$; for comparison, intrinsic widths of the lines of our interest are typically below 1 eV). Therefore the S/N at the energy of the line center, E_l , is estimated as

$$S/N(E_l) = \frac{[\mathcal{N}_0(E_l) - \mathcal{N}(E_l)]\Delta E}{\sqrt{\mathcal{N}(E_l)\Delta E}} \quad (23)$$

simply from the Poisson statistics of the observed photons.

We compute the equivalent width and the S/N of absorption line systems for 6400 random LOSs in the $5^\circ \times 5^\circ$ region assuming the number of photons described in §2.3. Figure 3 plots the cumulative number distribution of the equivalent width of absorption line systems per LOS ($z = 0.0 - 0.3$) from our mock observation for 10 strong lines (Table 1). On average, O VII (574 eV) is the most prominent line in terms of the equivalent width, and O VIII (654 eV) and Fe XVII (826 eV) are the next. Figure 4 shows the corresponding cumulative number distribution of S/N. Note that the value of S/N should be replaced by

$$\begin{aligned} S/N &= (S/N)_{\text{fiducial}} \left(\frac{F_0}{6 \times 10^{-13} [\text{erg s}^{-1} \text{cm}^{-2} \text{keV}^{-1}]} \right)^{1/2} \\ &= (S/N)_{\text{fiducial}} \left(\frac{\mathcal{N}_0(E = 500 \text{eV})}{5000 [\text{ph/eV}]} \right)^{1/2} \end{aligned} \quad (24)$$

if F_0 , and more generally the number of photons during the exposure time, \mathcal{N}_0 , are different from our fiducial values. In our adopted model for the GRB afterglow and the *XEUS* performance, O VII 574 eV and O VIII 654 eV lines achieve $S/N = 3$ when their equivalent widths are $W = 0.06 - 0.07$ eV and $W = 0.06 - 0.08$ eV, respectively, which provide the detection limit.

We find that the number of absorption systems which have $S/N \geq 3$ is 1.06/LOS (O VII 574 eV) and 0.23/LOS (O VIII 654 eV) as summarized in Table 2. Other lines exhibit below 0.1 systems/LOS. The number of the case that both O VII (574 eV) and O VIII (654 eV) exhibit $S/N \geq 3$ at the same position of WHIM is 0.21/LOS.

In order to check the dependence on the assumed metallicity model, we also consider two other metallicity models. One is a phenomenological model adopted in Paper II (the radiation pressure ejection model of 000 [cite]cite.Aguirre2001Aguirre et al.(2001)):

$$Z_{A,j}/Z_{A,\odot} = \min [0.2, 0.02(\rho_j/\bar{\rho}_b)^{0.3}], \quad (25)$$

where $\bar{\rho}_b$ is the mean baryon density at redshift z . The other adopts a constant metallicity comparable to the typical value for intra-cluster medium:

$$Z_{A,j} = 0.3Z_{A,\odot}. \quad (26)$$

Figure 5 shows the dependence of the cumulative number distribution of oxygen absorption line systems on the metallicity models; O VII (574eV) and O VIII (654eV) in thick and thin lines, respectively. Note that $Z_{A,j} > 0.1Z_{A,\odot}$ is satisfied only in relatively dense regions $\rho_j/\bar{\rho}_b > 214$ (eq. 25). This is why our fiducial model ($Z_{A,j} = 0.1Z_{A,\odot}$) has more absorption line systems than the model of equation 25.

3.2. Detectability of Oxygen Absorption Line Systems

Since the most prominent absorption lines detectable by *XEUS* are OVII and OVIII, we focus on these lines in what follows. Figure 6 shows column density maps of OVII (*Left panel*) and OVIII (*Right panel*) for $0 < z < 0.3$. As indicated in those panels, we select three different LOSs (A, B, and C). The mock spectra for those LOSs are shown in Figure 7; spectrum A exhibits many prominent absorption lines, and spectrum B has one strong line system while spectrum C has none.

We find two distinct absorption line systems which are located at $z = 0.12$ (marked by †) and $z = 0.29$ (marked by ‡) along the LOS of A; OVII ($z = 0.29$, $E = 445\text{eV}$, $W = 0.16\text{eV}$), OVIII ($z = 0.29$, $E = 507\text{eV}$, $W = 0.09\text{eV}$), OVII ($z = 0.12$, $E = 514\text{eV}$, $W = 0.10\text{eV}$), and OVIII ($z = 0.12$, $E = 585\text{eV}$, $W = 0.12\text{eV}$). Figure 8 is the column density map of OVII (*Left panels*) and OVIII (*Right panels*) but for $0.11 < z < 0.14$ (*Upper panels*) and for $0.26 < z < 0.30$ (*Lower panels*) so as to depict the WHIM responsible for the absorption systems in the spectrum A.

Figure 9 shows the mass-weighted (within each cell) temperature and the over-density distributions along the three LOSs. The top two panels for the region A have high over-density (10-100) and high temperature ($10^6 - 10^7\text{K}$) WHIM clumps at $z = 0.12$ and $z = 0.29$. They are indeed responsible for the prominent lines in the spectrum A of Figure 7. Spectrum B has one absorption system at $z = 0.22$ (OVII 574 eV $W = 0.06\text{eV}$) as indicated in Figures 8 and 9. In reality, however, the identification of the line redshift is very difficult with a single line. One may assume statistically that the strongest line in a single LOS should be that of OVII 574 eV, and then infer the redshift $574/470 - 1 = 0.22$. In this particular example, it turns out a correct guess, but may not work always. Finally spectrum C has no prominent absorption feature. Indeed Figure 9 shows that there is no region with over-density $\delta \equiv \rho/\bar{\rho} > 10$ along the LOS.

Figure 10 plots the distributions of mass-weighted temperatures and over-densities of WHIM averaged over each absorption line system of OVII (574 eV) and O VIII (654 eV). Consider an over-density profile along a LOS as schematically plotted in Figure 11. We define one connected clump enclosed between two boundaries with $\delta = 1$, and identify it as a single absorption line system. Then we compute its temperature and over-density by mass-weighted averaging over the relevant SPH particles within the entire line system.

The different symbols indicate the range of the equivalent width W of the absorption line systems; circles, crosses and triangles correspond to the systems with $W \geq 0.12\text{ eV}$, $0.07 \leq W \leq 0.12\text{ eV}$, and $0.05 \leq W \leq 0.07\text{ eV}$, respectively. Both OVII and O VIII can probe WHIM with $T > 10^6 - 10^7\text{ K}$ and over-density of $\delta = 10$ to 1000. WHIM with $T < 10^6\text{ K}$, however, can be traced only by O VII.

Figure 12 plots the fraction of gas contained in oxygen absorption line systems (O VII in *Upper panel* and O VIII in *Lower Panel*) which have the equivalent width larger than the specified value W . More specifically we first select all oxygen absorption line systems along the

i -th LOS whose equivalent width exceeds W , and sum up their hydrogen gas column densities. We denote the sum as $N_{H,i}^{\text{sim}}(> W)$. Then we take the following ratio averaged over 6400 LOSs:

$$R_H(> W) = \frac{\sum_{i=1}^{6400} N_{H,i}^{\text{sim}}(> W)}{\sum_{i=1}^{6400} N_{H,i}^{\text{sim}}(> 0)} \quad (27)$$

for O VII and O VIII separately. In reality this is an *unobservable* quantity, but provides a *simulated* gas mass fraction of oxygen absorption line systems which have a detectable line width. More importantly, this is the essential factor in properly estimating the total cosmic baryon density from the detected fraction of oxygens (§4.3).

Three shaded regions correspond to the temperature ranges $T > 10^7$ K, $10^6 < T < 10^7$ K, and $T < 10^6$ K from top to bottom. Comparison of the upper and lower panels suggest that OVIII tends to trace higher temperature regions than O VII. In the case of O VII (574 eV), we can detect only 21 % of baryon above the detection limit ($W \sim 0.06$ eV; §3.1). The region of $T > 10^7$ K accounts for 20 % of detectable baryons, which may be located in virialized regions like intra-cluster medium, and thus may be already detected through their thermal bremsstrahlung. The regions of $10^6 < T < 10^7$ K and $T < 10^6$ K account for 70 % and 10 % of detectable baryons, which can be regarded as WHIM. Note that one can detect the absorption lines of O VII (574eV) with $T < 10^6$ K, while it is almost impossible to find their emission counterparts (000 [cite]cite.Yoshikawa2003Yoshikawa et al.(2003)).

4. Spectral Diagnostics of Physical Properties of WHIM

4.1. OVII and OVIII Absorption Lines

As we have seen, the most prominent absorption lines are OVII (574 eV) and OVIII (654 eV). On average, 21 % of random LOSs have an intervening clump of WHIM which exhibits both absorption lines with $S/N \geq 3$. In this case, the ratio of their equivalent widths should provide the temperature of the WHIM *in principle*. Consider a clump of WHIM which has a uniform temperature T and density ρ , then the ratio of the equivalent widths is written as

$$\frac{W_{\text{OVII},574\text{eV}}}{W_{\text{OVIII},654\text{eV}}} \sim \frac{f_{\text{OVII},574\text{eV}} F_{\text{OVII}}(T, \rho)}{f_{\text{OVIII},654\text{eV}} F_{\text{OVIII}}(T, \rho)}, \quad (28)$$

where f is the oscillator strength and F is the ionization fraction. The WHIM which exhibits OVIII (654 eV) absorption has temperature of $10^6 - 10^7$ K (Fig.10). In this temperature range, the ionization fraction approaches the value in CIE, and the ratio of the oxygen equivalent widths, eq.(28), is expected to be insensitive to the density, ρ .

Figure 13 provides the scatter plot of the ratio of O VII and O VIII equivalent width versus the mass-weighted average temperature for systems where which both O VII (574 eV) and O VIII (654 eV) exhibit $S/N \geq 3$. Three solid lines indicate the theoretical curves in Eq.

(28) applying different hydrogen number density $n_H = 10^{-5}$, 10^{-6} , and 10^{-7} cm^{-3} from top to bottom. Inhomogeneous density and temperature structures are responsible for the departure from the theoretical model which assumes uniform distribution. Figure 14 shows an example of sub-structure in a simulated absorption line system. Temperature is highest near the center of the clump, and over-density is also high. Therefore, ionization fractions of OVII and OVIII are rather suppressed. This anti-correlation of oxygen abundances inside the inhomogeneous distribution of WHIMs explains why the simulated systems in Figure 13 preferentially lie at higher temperature regime than the theoretical prediction.

4.2. Combined Analysis with the Emission Lines

The absorption line analysis discussed so far can be applied to bright QSOs as well. The advantage of the GRB afterglow observation, however, lies in the fact that the follow-up survey of the same region by a small X-ray satellite like *DIOS* may be able to identify the emission line counterparts of the absorption systems. We consider the feasibility in detail here.

Figure 15 shows the mock emission spectrum of the region A in Figures 6 to 9. We assume the exposure time $T_{\text{exp}} = 10^6$ sec with *DIOS* for its 1 pixel ($\Delta\omega = 1/256$ deg^2). A strong line around $E = 510$ eV is the emission line of OVIII (654 eV) from the WHIM at $z = 0.29$. The lines around 585 eV and 640 eV correspond to OVIII (654 eV) and Fe XVII (826 eV) from WHIM at $z = 0.12$ (see also Fig. 9).

We estimate the signal-to-noise ratio of the emission lines as

$$(S/N)_l = \frac{\left(\frac{\bar{f}_{\text{em}}(E_l) S_{\text{eff}} \Delta\omega T_{\text{exp}}}{E_l} \right)}{\sqrt{\left(\frac{J_B(E_l) \Delta E S_{\text{eff}} \Delta\omega T_{\text{exp}}}{E_l} \right) + \left(\frac{\bar{f}_{\text{em}}(E_l) S_{\text{eff}} \Delta\omega T_{\text{exp}}}{E_l} \right)}}, \quad (29)$$

where $\bar{f}_{\text{em}}(E_l)$ [erg/s/cm²/sr] is the total flux of the emission line centered at $E = E_l$ averaged over the 1 pixel of the detector, and $J_B(E_l)$ [erg/s/cm²/sr/eV] is the sum of the energy spectra of CXB and UVB, Eqs. (8) and (9).

Table 3 shows the number of the various case of the observable emission lines with the absorption lines. In Table 3, “yes” shows $S/N \geq 3$ and “no” indicates $S/N < 3$. We find that we can identify the OVII (574 eV) or OVIII (654 eV) emission lines in approximately 20 % of the detected oxygen absorption line systems.

If a clump of WHIM responsible for one absorption system has a uniform density ρ and uniform temperature T , the surface brightness of the line for the ion species A^{n+} is

$$S_A \propto \frac{\rho^2 \epsilon(T, \rho, Z_A)}{(1+z)^4} \frac{\Delta V}{d_A(z)^2 \Delta\omega}, \quad (30)$$

and its equivalent width (in the observer’s frame) is

$$W_A \propto \frac{\rho A^{n+}}{1+z} \Delta L, \quad (31)$$

where ΔV and ΔL denote a volume and a path length of the clump of WHIM. In the uniform distribution, $\Delta V/d_A^2(z)\Delta\omega$ is simply equal to ΔL . Because $\epsilon(T, \rho, Z_A) \propto Z_A$ and $\rho_{A^{n+}} \propto Z_A \rho$, $S_A(1+z)^3/W_A$ is approximately proportional to ρ . Thus one expects to infer ρ in principle without prior knowledge of the metallicity Z_A if the temperature T can be reliably obtained by the ratio of OVII and OVIII absorption lines or emission lines. In reality, however, actual density and temperature distributions are fairly inhomogeneous as shown in Figure 14. Thus the density and temperature determination using OVII and OVIII lines is subject to large uncertainties. Therefore it seems unlikely that the follow-up emission survey will add particularly important information to the detected absorption line systems. Nevertheless successful detections of both absorption and emission features will offer unambiguous evidence of the presence of WHIM at the redshift.

4.3. Reliability of estimate of Ω_b from WHIM observations

If absorption lines of WHIM are detected along a particular line of sight, one would naturally attempt to estimate the contribution of WHIM to the total cosmic baryon density, Ω_b^{WHIM} . [Nicastro et al. \(2005\)](#) ([Nicastro et al. \(2005\)](#)) indeed reported $\Omega_b^{\text{WHIM}} = (2.7_{-1.9}^{+3.8}\%) \times 10^{-[\text{O}/\text{H}]-1}$ using two absorption lines. We examine the reliability of this procedure using our mock data.

Let us first define the estimated fraction of WHIM with signal-to-noise ratio exceeding a given threshold, S/N , along one LOS as follows:

$$\Omega_{\text{gas}}^{\text{WHIM,est}}(> S/N) = \frac{1}{d_c(z=0.3)\rho_c} \sum_i \frac{N_{H,i}^{\text{est}}(> S/N)}{X(1+z_i)^2}, \quad (32)$$

$$N_{H,i}^{\text{est}}(> S/N) = \frac{N_{\text{OVII},i}(> S/N)}{F_{\text{OVII},i}(T)} \left(\frac{n_H}{n_O} \right) \quad (33)$$

where i denotes an index for absorption line systems, $X (= 0.755)$ is the hydrogen mass fraction, and $d_c(z=0.3)$ is the comoving distance from $z=0$ to $z=0.3$. We convert the observed equivalent width into $N_{\text{OVII}}(> S/N)$ using Eq. (22) assuming that the line is in its linear regime of the growth curve. We focus on the case in which both O VII and O VIII are detected. Then we estimate temperature T using Eq. (28) and derive the ionization fraction $F_{\text{OVII}}(T)$ assuming collisional ionization equilibrium. If we multiply the hydrogen-to-oxygen number ratio, we have an estimate of the hydrogen column density for the i -th absorption line system, $N_{H,i}^{\text{est}}(> S/N)$. In practice, we adopt $(n_O/n_H) = 0.1(n_O/n_H)_\odot = 10^{-4.07}$ ([Anders & Grevesse \(1989\)](#)). Finally this is converted to the density parameter of gas, $\Omega_{\text{gas}}^{\text{WHIM,est}}(> S/N)$ responsible for absorption exceeding the detection S/N .

Apart from the metallicity, $N_{H,i}^{\text{est}}(> S/N)$ is observable. As we have seen in the previous sections, however, the inhomogeneity of the temperature and density within one absorption system would result in a systematic underestimate. In order to check the systematic effect as well as the assumption of CIE in equation (33) (while we did adopt CIE in creating mock

spectra from simulation data), we compare $N_{H,i}^{\text{est}}(> S/N)$ with $N_{H,i}^{\text{sim}}(> S/N)$ directly computed from simulation data (§3.2). Figure 16 clearly shows the degree of the underestimate bias.

In order to estimate the total baryon density, Ω_b^{est} , from $\Omega_{\text{gas}}^{\text{WHIM,est}}(> S/N)$, we have to correct for (i) the fraction of gas below the detection limit, (ii) the fraction of stars in galaxies, and (iii) the above systematic bias. Therefore we write the estimate as

$$\Omega_b^{\text{est}} = \frac{\Omega_{\text{gas}}^{\text{WHIM,est}}(> S/N)}{R_H(> S/N)} \frac{f_{\text{gas}} + f_{\text{star}}}{f_{\text{gas}}} \left\langle \frac{N_H^{\text{sim}}(> S/N)}{N_H^{\text{est}}(> S/N)} \right\rangle. \quad (34)$$

In practice, we choose $S/N = 3$ in the following. We compute the fraction of WHIMs which exhibit both OVII and OVIII absorptions (similarly as in Figure 12), and find $R_H(> 3\sigma) = 0.12$. As for the second factor, we evaluate directly from simulations; $f_{\text{gas}} = 0.79$ and $f_{\text{star}} = 0.21$. As Figure 16 indicates, the last correction factor significantly varies and it is not easy to choose a relevant average value. If we adopt the mean value as plotted in triangles, $\langle N_H^{\text{sim}}(> 3\sigma)/N_H^{\text{est}}(> 3\sigma) \rangle \sim 1/4$. Adopting those correction factors, we plot the histogram of Ω_b^{est} in Figure 17.

Upper panel is the case where both OVII and OVIII absorptions are detected (1197 LOSs out of 6400 LOSs). The mean value of the resulting Ω_b^{est} averaged over the entire LOSs (even including the non-detected 5203 LOSs) amounts to 0.025 (plotted in the dotted line). This is in reasonable agreement with the value adopted in the simulation, 0.03. On the other hand, it clearly demonstrates the fact that any estimate based on the positive detection alone may significantly overestimate the real value; it is essential to take account of the above correction factors properly.

Lower panel in Figure 17 indicates the 4248 LOSs along which only O VII absorption lines are detected. In this case, one has to assume the temperature *a priori*, and we show results for $T = 10^{5.5}$, $10^{6.0}$, and $10^{6.5}$ K. The temperature dependence is very strong and even not monotonic. This reflects the strong dependence of OVII fraction on temperature as exhibited in Figure 1. The two peaks in the histogram correspond to LOSs which have single and double absorption line systems. Therefore unless one can reliably estimate the temperature, it is difficult to estimate the cosmic baryon density from the O VII absorption line observations alone.

5. Conclusions and Discussion

In this paper, we have examined the detectability of WHIM via the absorption lines in a bright GRB afterglow spectra using the cosmological hydrodynamic simulation. We created the mock *XEUS* absorption spectra toward a strong GRB afterglow assuming the collisional and photo-ionization equilibrium. We conclude that on the average *XEUS* will detect 1.06 (O VII 574 eV) and 0.23/ (O VIII 654 eV) per a random line-of-sight up to $z = 0.3$ ($S/N \geq 3$). Unfortunately it is not easy to find the emission line counterpart for such absorption systems (less than 20% chance for $Z = 0.1Z_{\odot}$; see Table 3). In a sense, this makes a strong case for the complementary role of the WHIM emission survey with a small dedicated X-ray mission like

DIOS, quite independently of the absorption line search with *XEUS*.

If both OVII and OVIII absorptions are detected ($\sim 20\%$ chance) for the same WHIM clump, one can estimate its temperature from their line ratios and attempt to infer the cosmic baryon density. As we discussed in detail, however, the reliable estimate requires several careful correction factors and still the resulting distribution function of the estimate is fairly wide. So any attempt on the basis of small statistical samples should be interpreted with caution.

In passing we have to emphasize once again that our simulation data adopted $\Omega_b = 0.03$ rather than the currently more favored value 0.04. Also we restrict our current analysis up to $z = 0.3$ where a spectrum is relatively free from the Galactic confusion, but in principle one can explore WHIM systems at higher redshifts ($z \sim 1$) with GRB. Therefore while our present conclusions concerning the detectability of WHIM in absorption toward a GRB may seem fairly modest, most likely they are very conservative. Moreover the result is very sensitive to the metallicity of WHIM which is rather uncertain and is likely to significantly vary from place to place. Given the strong metallicity dependence as shown in Figure 5, what is relevant is not the mean metallicity of WHIM but the fraction of WHIM clumps which exhibit detectable equivalent width. In this respect, the wide variation of the metallicity, even if its overall mean is $0.1Z_\odot$ as we most adopted here, is expected to *systematically* increase the detectability.

In order to be more quantitative, we need much more advanced simulation datasets which include more realistic physical processes such as radiative cooling, photo-ionization, star formation, supernova feedback, and metallicity evolution. This is exactly what we are performing, and we hope to revisit the above issues in due course.

Numerical computations presented in this paper were carried out at ADAC (the Astronomical Data Analysis Center) of the National Astronomical Observatory, Japan (project ID: mky05a). We are also grateful to Kei Hiraki and Mari Inaba for their generous allocation of computer resources at the University of Tokyo supported by the Special Coordination Fund for Promoting Science and Technology, Ministry of Education, Culture, Sport, Science and Technology. This work was supported in part by Grants-in-Aid for Scientific Research from the Japan Society for Promotion of Science (Nos.14102004, 14204017, 15340088, 15740157, and 16340053).

References

- [Aguirre et al.(2001)] Aguirre, A., Hernquist, L., Schaye, J., Katz, N., Weinberg, D.H., & Gardner, J. 2001, ApJ, 561, 521
- [Anders & Grevesse(1989)] Anders, E., & Grevesse, N. 1989, Geochim. Cosmochim. Acta, 53, 197
- [Cen & Ostriker(1999a)] Cen, R. & Ostriker, J. 1999a, ApJ, 514, 1
- [Cen & Ostriker(1999b)] Cen, R. & Ostriker, J. 1999b, ApJ, 519, L109
- [Chen et al.(2003)] Chen, X., Weinberg, D.H., & Davé, R. 2003, ApJ, 594, 42

- [Davé et al.(2001)] Davé, R., Cen, R., Ostriker, J.P., Bryan, G.L., Hernquist, L., Katz, N., Weinberg, D.H., Norman, M.L., & O’Shea, B. 2001, *ApJ*, 552, 473
- [Fang, Bryan, Canizares(2002)] Fang, T., Bryan, G.L., & Canizares, C.R. 2002, 564, 604
- [Fang et al.(2002)] Fang, T., Marshall, H.L., Lee, J.C., Davis, D.S., & Canizares, C.R., 2002, *ApJ*, 572, L127
- [Fiore et al.(2000)] Fiore, F., Nicastro, F., Savaglio, S., Stella, L., & Vietri, M., 2000, *ApJ*, 544, L7
- [Fukugita, Hogan, & Peebles(1998)] Fukugita, M., Hogan, C.J., & Peebles, P.J.E. 1998, *ApJ*, 503, 518
- [Fukugita & Peebles(2004)] Fukugita, M., & Peebles, P.J.E. 2004, *ApJ*, 616, 643
- [Fujimoto et al.(2004)] Fujimoto, R., Takei, Y., Tamura, T., Mitsuda, K., Yamasaki, N.Y., Shibata, R., Ohashi, T., Ota, N., Audley, M.D., Kelley, R.L., Kilbourne, C.A., 2004, *PASJ*, 56, L29
- [Jager et al 1997] Jager, R., Mels, W. A., Brinkman, A. C., Galama, M. Y., Goulooze, H., Heise, J., Lowes, P., Muller, J. M., Naber, A., Rook, A., Schuurhof, R., Schuurmans, J. J., Wiersma, G., 1997, *A&A S*, 125, 557
- [Kang et al.(2005)] Kang, H., Ryu, D., Cen, R., Song, D., 2005, *ApJ*, 620, 21
- [Morrison & McCammon(1983)] Morrison R. & McCammon D., 1983, *ApJ*, 270, 119
- [Mewe, Gronenschild, & van den Oord(1985)] Mewe, R., Gronenschild, E.H.B.M., & van den Oord, G.H.J., 1985, *A&A S*, 62. 197
- [Miyaji et al.(1998)] Miyaji, T., Ishisaki, Y., Ogasaka, Y., Ueda, Y., Freyberg, M. J., Hasinger, G., & Tanaka, Y. 1998, *A&A*, 334, 13
- [Mathur et al.(2003)] Mathur, S., Weinberg, D.H., & Chen, X. 2003, *ApJ*, 582, 82
- [Nicastro et al.(2002)] Nicastro, F., Zezas, A., Drake, J., Elvis, M., Fiore, F., Fruscione, A., Marengo, M., Mathur, S., & Bianchi, S. 2002, *ApJ*, 573, 157
- [Nicastro et al.(2005)] Nicastro, F., Mathur, S., Elvis, M., Drake, J., Fang, T., Fruscione, A., Krongold, Y., Marshall, H., Williams, & R., Zezas, A. 2005, *Nature*, 433, 495
- [Ohashi et al.(2003)] Ohashi, T. et al. in Proceedings of “Modelling the Intergalactic and Intracluster Media” (astro-ph/0402546)
- [Piro (2004)] Piro, L., 2004, *ASP Vol.312 / astro-ph 0402638*
- [Shull et al.(1999)] Shull, J.M., Roberts, D., Giroux, M.L., Penton, S.V., & Fardal, M.A. 1999, *AJ*, 118, 1450
- [Spergel et al.(2003)] Spergel, D. N. et al. 2003, *ApJS*, 148, 175
- [Suto et al.(2004a)] Suto, Y., Yoshikawa, K., Yamasaki, N.Y., Mitsuda, K., Fujimoto, R., Furusho, T., Ohashi, T., Ishida, M., Sasaki, S., Ishisaki, Y., Tawara, Y., Furuzawa, A. 2004a, *Journal of the Korean Physical Society*, 45, S110
- [Suto et al.(2004b)] Suto, Y., Yoshikawa, K., Dolag, K., Sasaki, S., Yamasaki, N.Y., Ohashi, T., Mitsuda, K., Tawara, Y., Fujimoto, R., Furusho, T., Furuzawa, A., Ishida, M., Ishisaki, Y., Takei, Y. 2004b, *Journal of the Korean Astronomical Society*, 37, 387
- [Tripp, Savage & Jenkins(2000)] Tripp, T.M., Savage, B.D., & Jenkins, E.B. 2000, *ApJ*, 534, L1
- [Verner et al.(1996)] Verner, D.A., Verner, E.M., & Ferland, G.J. 1996, *Atomic Data Nucl. Data Table*, 64, 1
- [Yoshikawa et al.(2001)] Yoshikawa, K., Taruya, A., Jing, Y.P., & Suto, Y. 2001, *ApJ*, 558, 520
- [Yoshikawa et al.(2003)] Yoshikawa, K., Yamasaki, N.Y., Suto, Y., Ohashi, T., Mitsuda, K., Tawara,

Y., Furuzawa, A. 2003, PASJ, 55, 879 (Paper I)

[Yoshikawa et al.(2004)] Yoshikawa, K., Dolag, K., Suto, Y., Sasaki, S., Yamasaki, N.Y., Ohashi, T., Mitsuda, K., Tawara, Y., Fujimoto, R., Furusho, T., Furuzawa, A., Ishida, M., Ishisaki, Y., & Takei, Y. 2004, PASJ, 56, 939 (Paper II)

[Zhang et al.(1997)] Zhang, Y., Anninos, P., Norman, M. L., & Meiksin, A. 1997, ApJ, 485, 496

Table 1. Ten prominent resonant absorption lines in 0.3 – 1.5 keV

species	energy	oscillator strength
CVI	368 eV	0.416
NVI	431 eV	0.675
NVII	500 eV	0.416
OVII	574 eV	0.696
OVII	666 eV	0.146
OVIII	654 eV	0.416
NeIX	922 eV	0.724
Nex	1022 eV	0.416
MgXI	1352 eV	0.742
FeXVII	826 eV	2.96

Table 2. Expected number of oxygen absorption line systems with $S/N \geq 3$ and $S/N \geq 2$ per LOS up to $z = 0.3$.

metallicity model		expected number/LOS		
		OVII (574 eV)	OVIII (654 eV)	OVII and OVIII
$Z = 0.1Z_{\odot}$	$S/N \geq 3$	1.06	0.23	0.21
	$S/N \geq 2$	2.18	0.57	0.54
$Z = \min[0.2, 0.02(\rho/\bar{\rho})^{0.3}]Z_{\odot}$	$S/N \geq 3$	0.33	0.10	0.09
	$S/N \geq 2$	0.69	0.22	0.20
$Z = 0.3Z_{\odot}$	$S/N \geq 3$	5.10	1.67	1.59
	$S/N \geq 2$	8.11	2.73	2.48

Table 3. Fraction of oxygen absorption lines (O VII 574 eV, O VIII 654 eV) which exhibit the emission counterpart in 1 pixel size ($1/256 \text{ deg}^2$) of *DIOS*. The word “yes” shows $S/N \geq 3$ and “no” indicates $S/N < 3$, respectively. The column of N/LOS indicates the number of these combinations per LOS up to $z = 0.3$.

absorption		emission		$Z = 0.1Z_{\odot}$		$Z = \min[0.2, 0.02(\rho/\bar{\rho})^{0.3}]Z_{\odot}$	
O VII	O VIII	O VII	O VIII	N/LOS	%	N/LOS	%
yes	yes	yes	yes	0.029	3	0.026	8
yes	yes	yes	no	0.000	0	0.000	0
yes	yes	no	yes	0.066	6	0.033	10
yes	no	yes	yes	0.024	2	0.015	4
yes	no	yes	no	0.000	0	0.000	0
yes	no	no	yes	0.085	8	0.050	14
no	yes	yes	yes	0.003	0.3	0.009	2
no	yes	yes	no	0.000	0	0.000	0
no	yes	no	yes	0.008	0.7	0.007	2
yes	yes	no	no	0.111	11	0.026	8
yes	no	no	no	0.721	69	0.180	52
no	yes	no	no	0.002	0.2	0.000	0

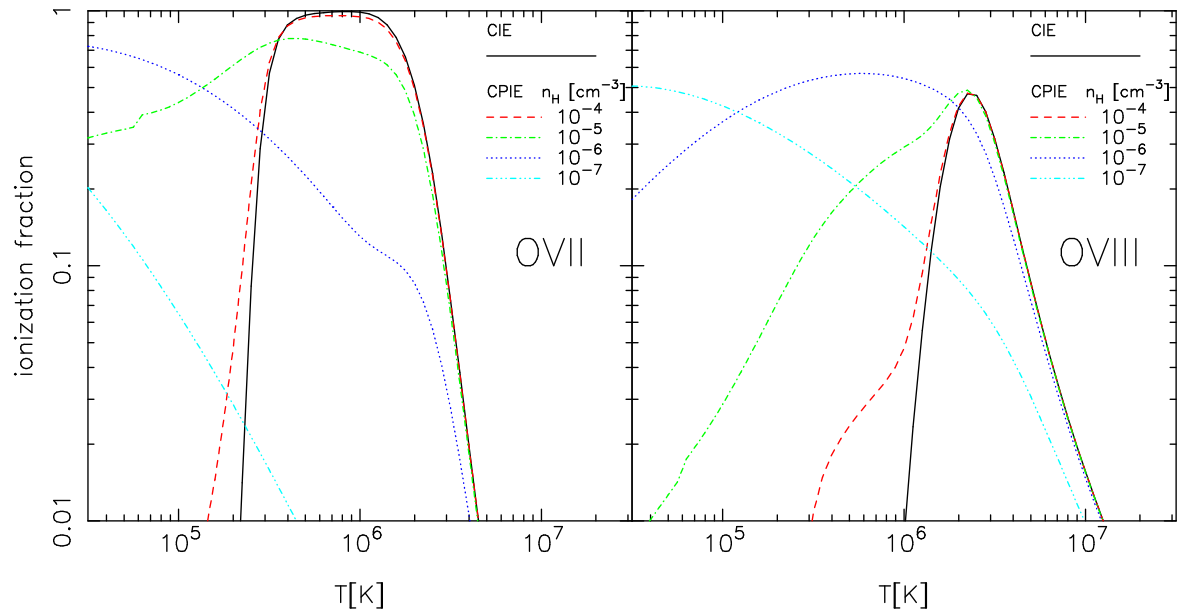


Fig. 1. Ionization fraction of OVII and OVIII as a function of temperature; CIE for solid lines and CPIE for the other lines (adopting $n_H = 10^{-4}, 10^{-5}, 10^{-6}$ and 10^{-7} cm⁻³).

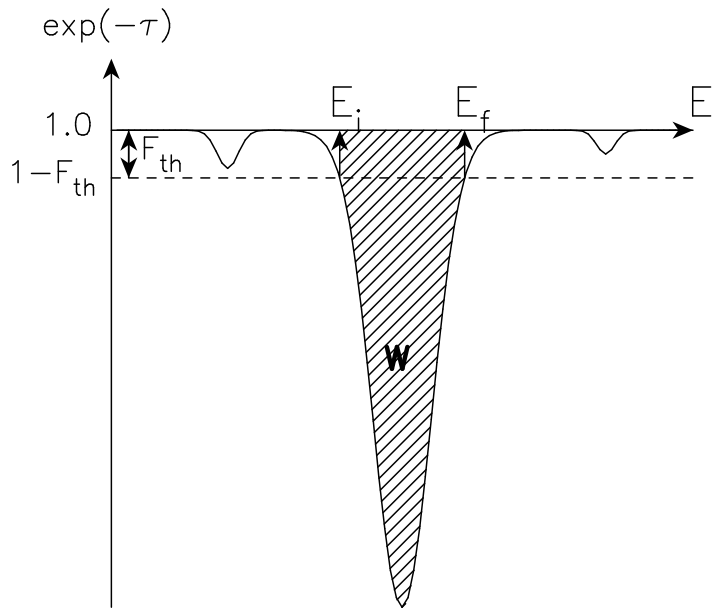


Fig. 2. Schematic identification method of absorption lines.

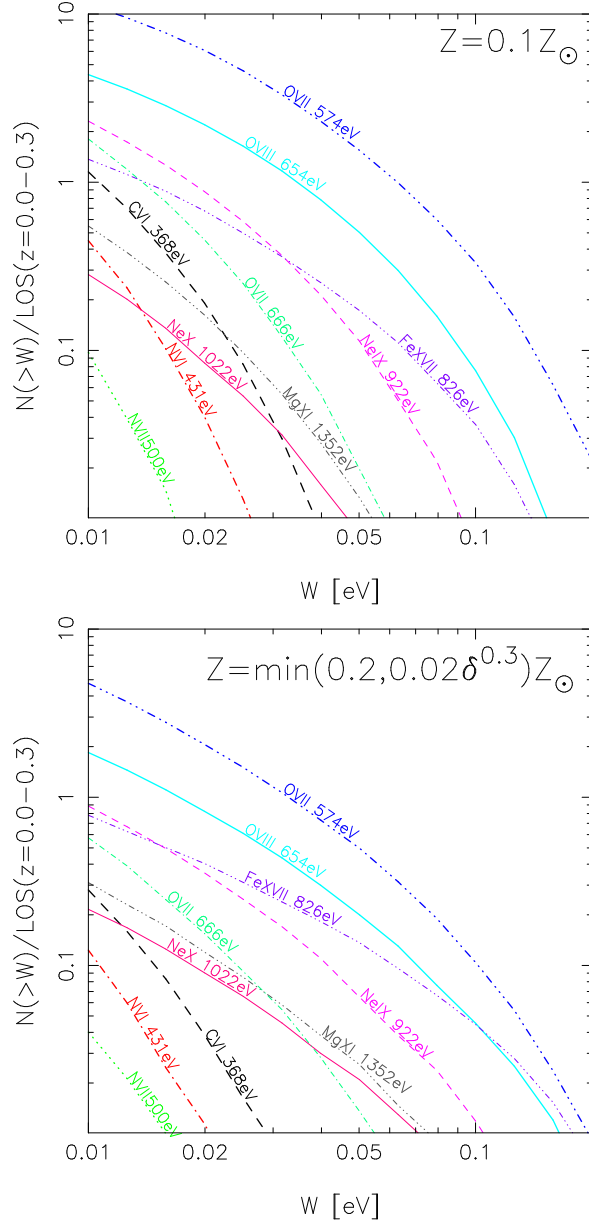


Fig. 3. Cumulative distribution of expected number of absorption line systems for $0 < z < 0.3$ as a function of their equivalent width; *Upper panel* $Z = 0.1Z_{\odot}$, *Lower panel* $Z/Z_{\odot} = \min[0.2, 0.02(\rho/\bar{\rho}_b)^{0.3}]$.

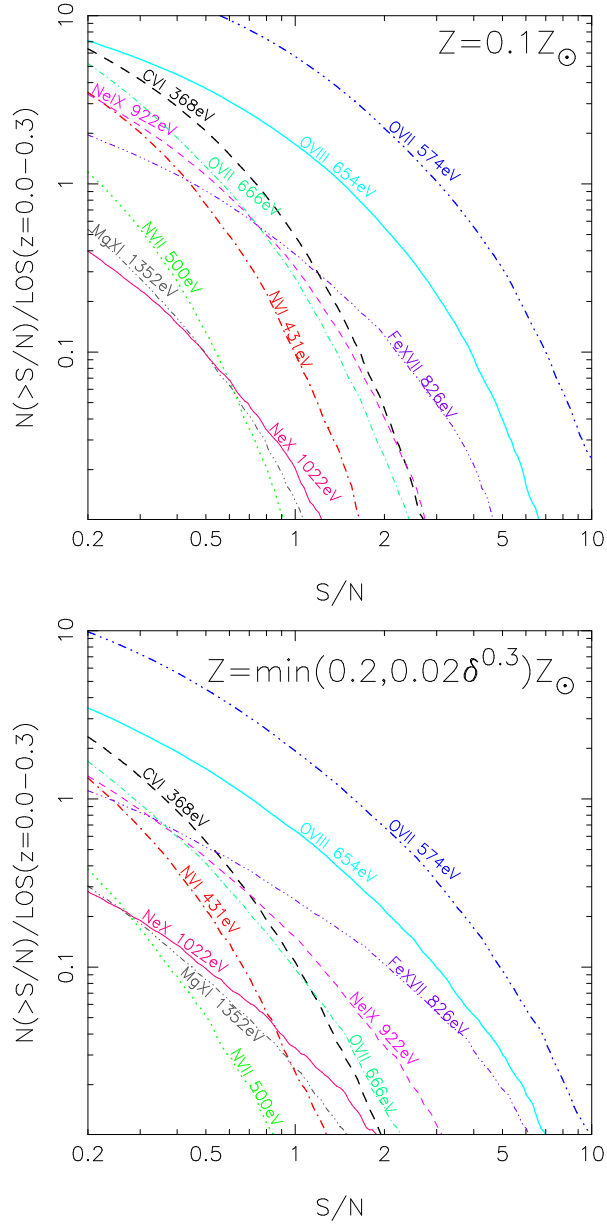


Fig. 4. Cumulative distribution of expected number of absorption line systems for $0 < z < 0.3$ as a function of their detection signal-to-noise ratios. The plots are converted from those of Fig. 3 assuming the *XEUS* observation toward a GRB afterglow discussed in §2.3.

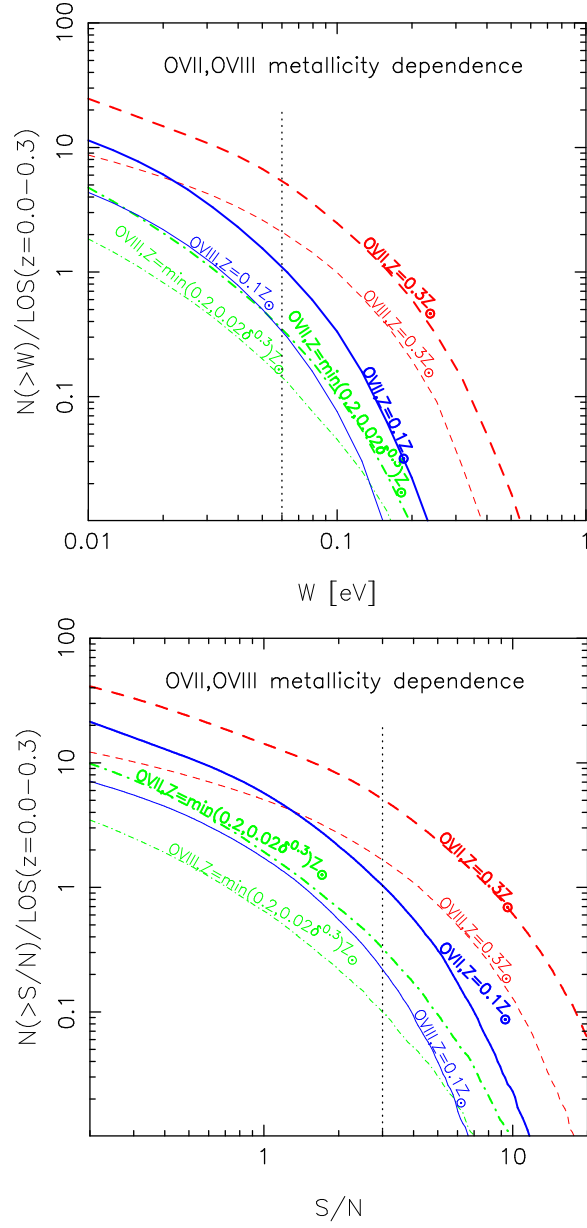


Fig. 5. Cumulative distribution of OVII and OVIII absorption lines for different metallicity models as a function of W (*Upper panel*) and S/N (*Lower panel*). Dotted lines indicate our fiducial detection limits; $W = 0.06\text{eV}$ and $S/N = 3$

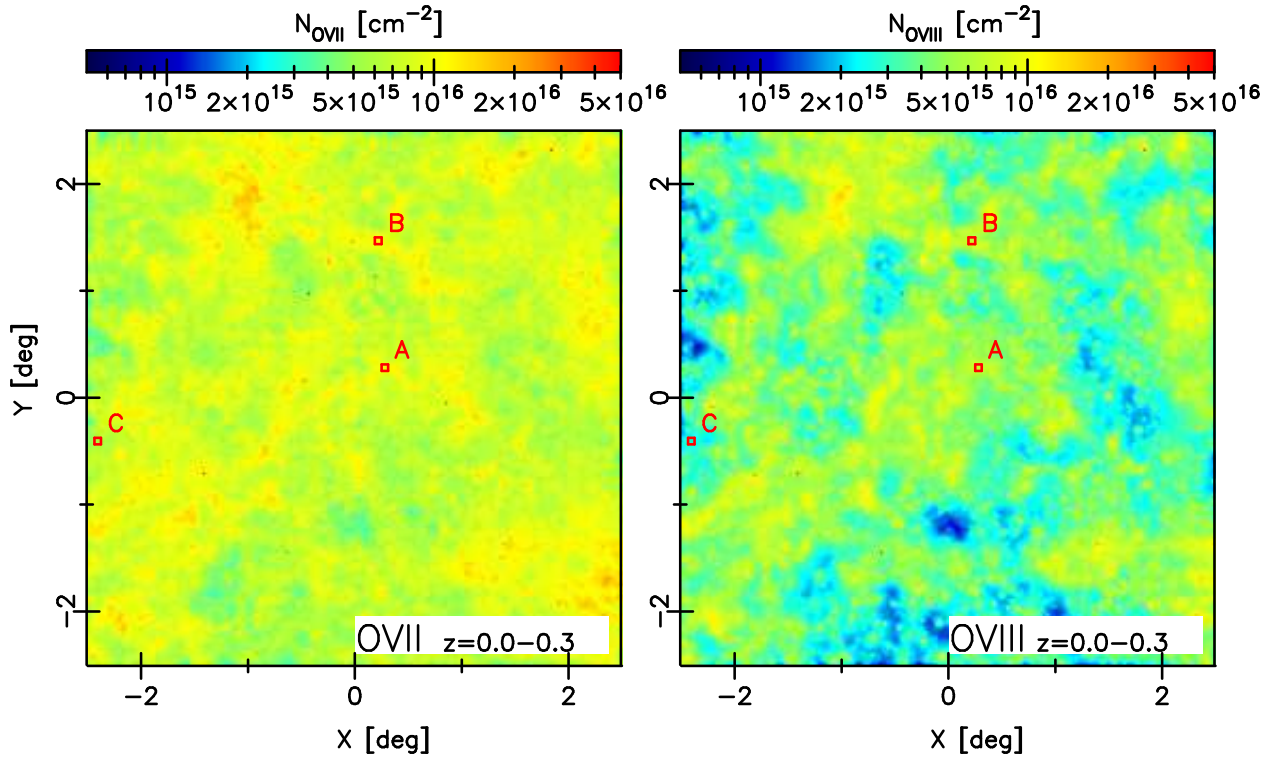


Fig. 6. Column density map of OVII (*Left panels*) and OVIII (*Right panels*) for $0.0 < z < 0.3$. Three red squares labeled A, B and C indicate the regions corresponding to Figures 7 to 9.

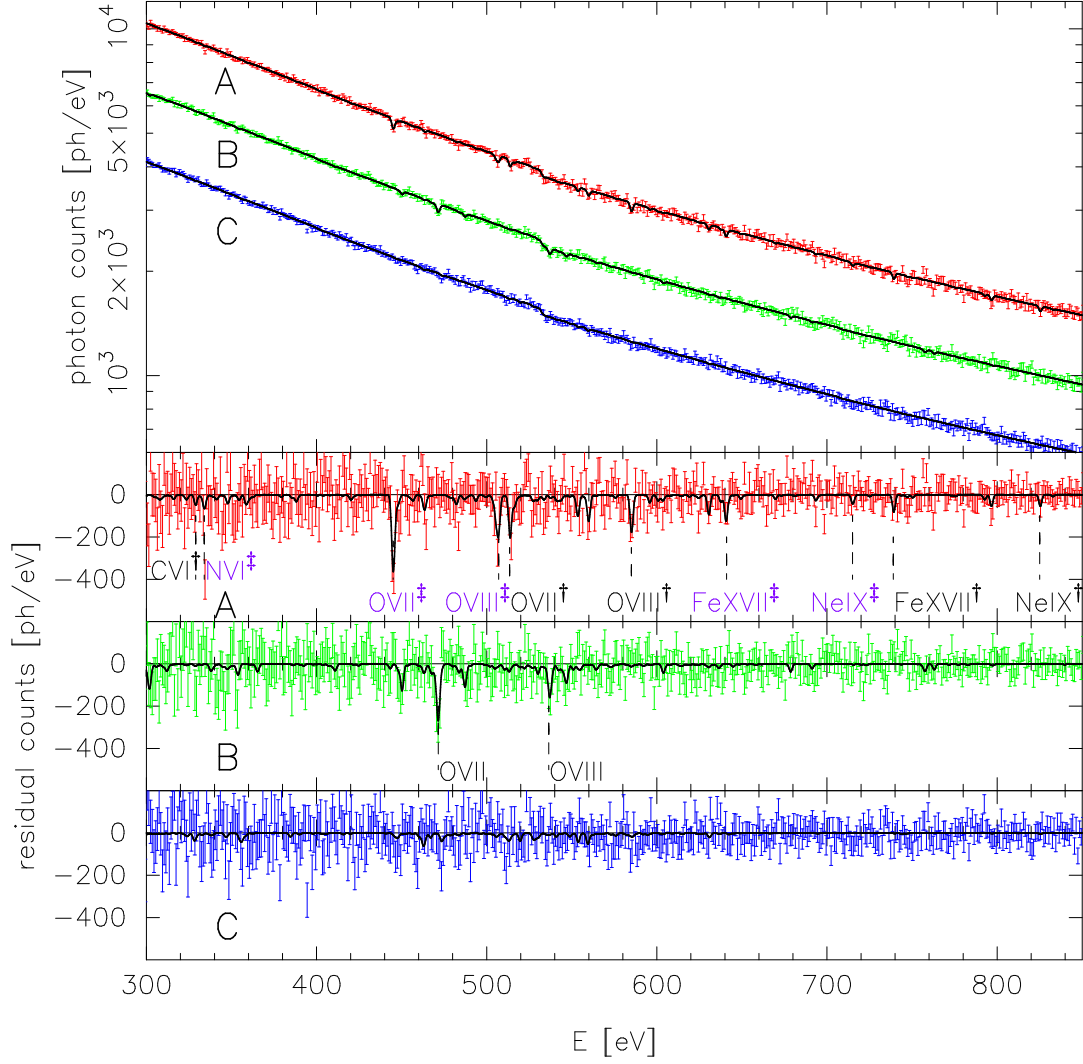


Fig. 7. Mock transmission spectra of a GRB afterglow. Top panel plots the photon counts through three different LOSs (A, B and C indicated in Figure 6). For an illustrative purpose, curves B and C are artificially multiplied by a factor of $10^{-0.2}$ and $10^{-0.4}$. Lower panels show their residual counts normalized by the continuum level. The metal line systems with labels † and ‡ in the spectrum A correspond to the WHIM clumps at $z = 0.12$ (*upper panels* in Fig.8) and $z = 0.29$ (*lower panels* in Fig.8), respectively.

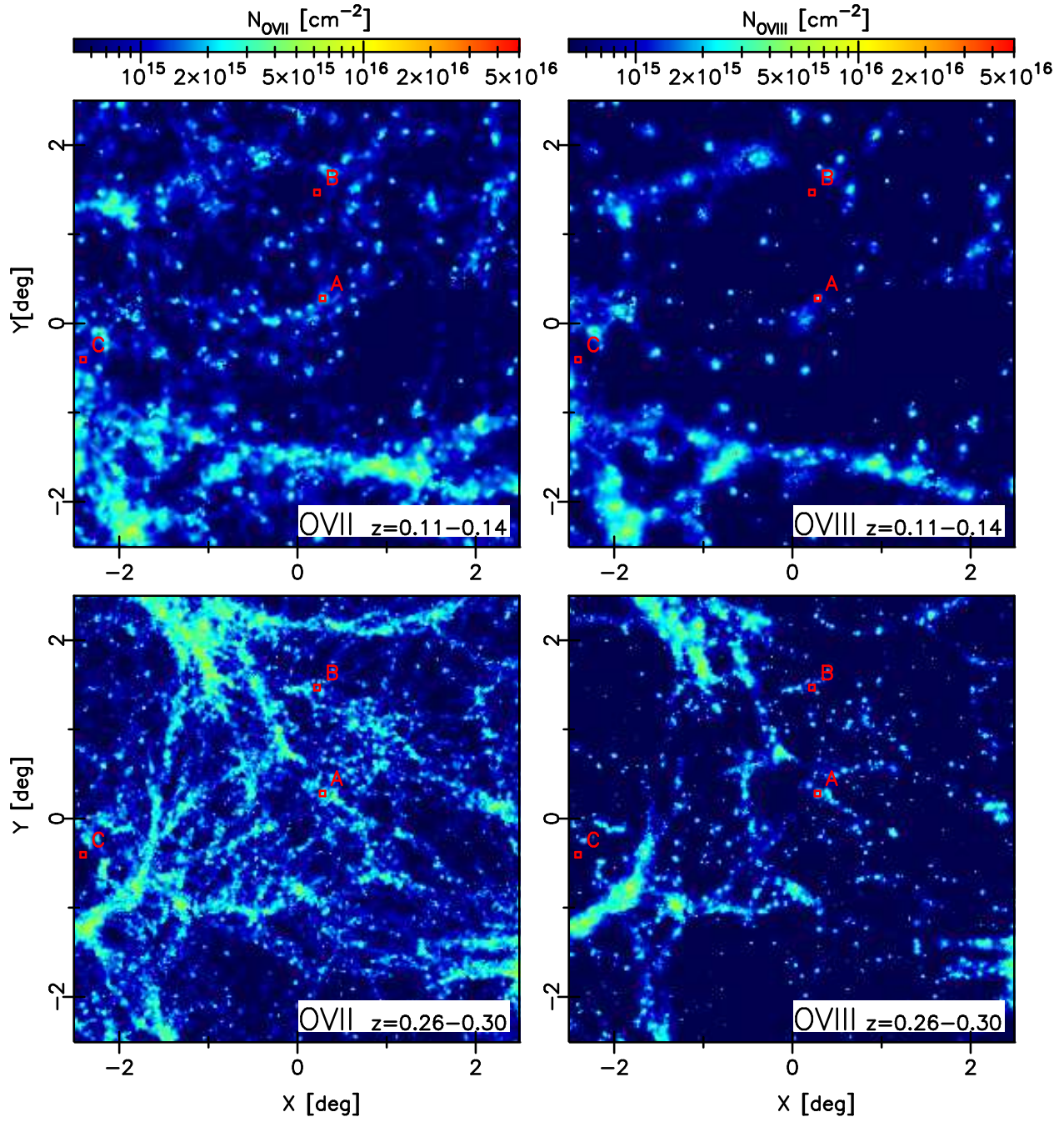


Fig. 8. Same as Figure 6, but for $0.11 < z < 0.14$ (upper panels) and for $0.26 < z < 0.30$ (lower panels).

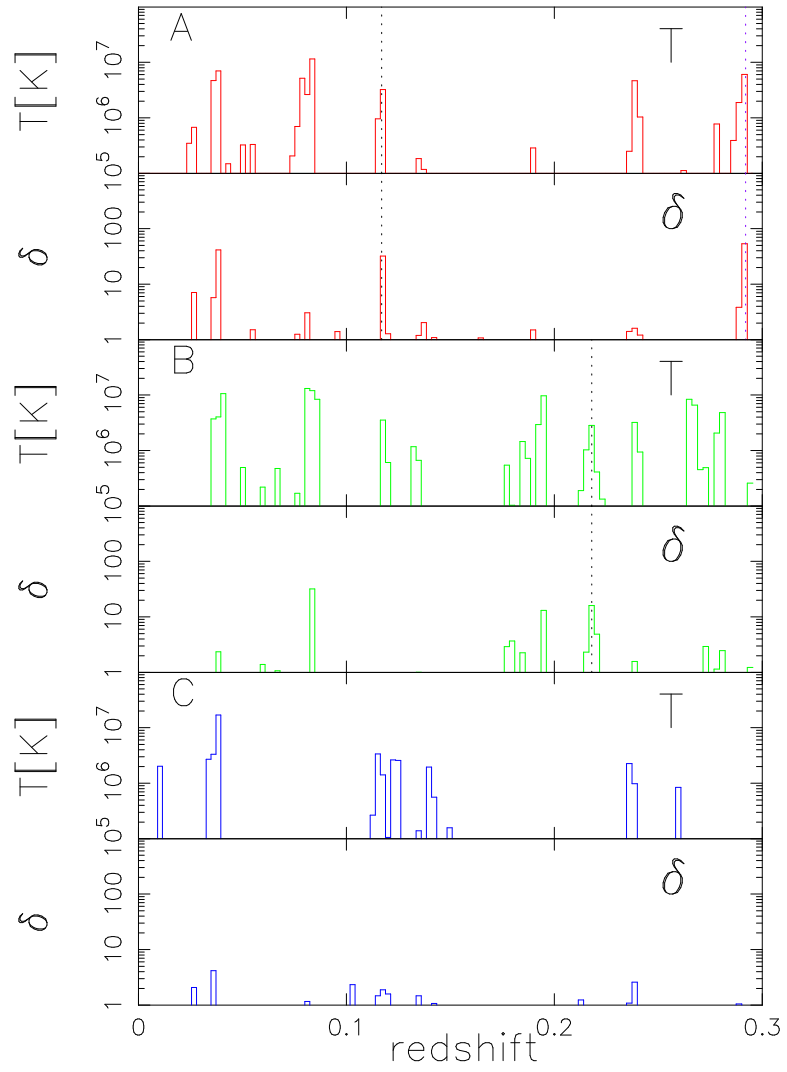


Fig. 9. Redshift distribution of temperature and over-density along the three LOSs A, B and C (from top to bottom).

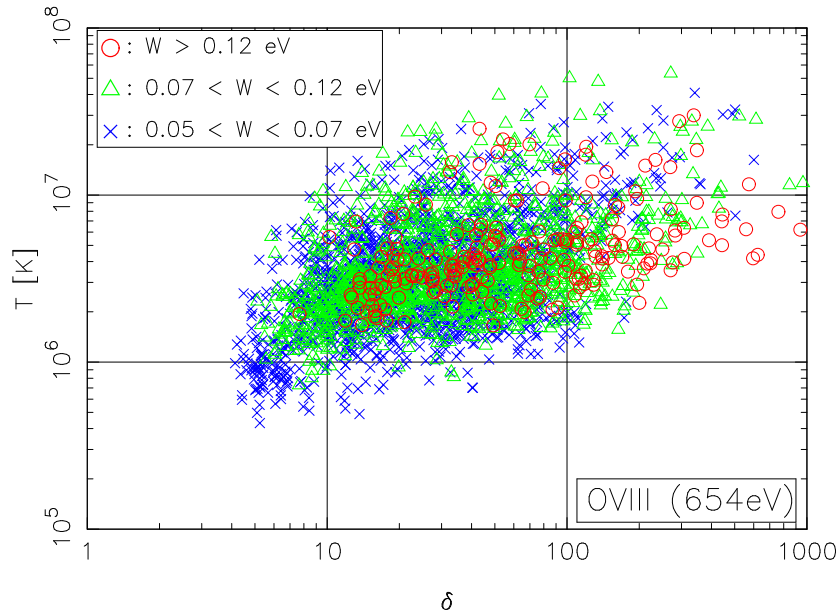
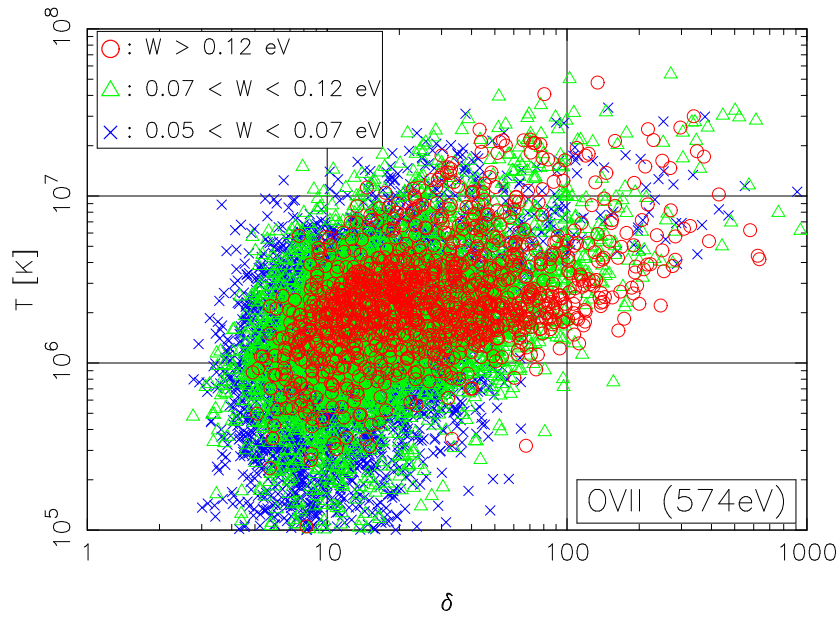


Fig. 10. Scatter plots of over-density and temperature of absorption line systems; OVII 574 eV (*upper panel*) and O VIII 654 eV (*lower panel*). Circles, crosses and triangles correspond to the systems with equivalent width of $W \geq 0.12$ eV, $0.07 \leq W \leq 0.12$ eV, and $0.05 \leq W \leq 0.07$ eV, respectively.

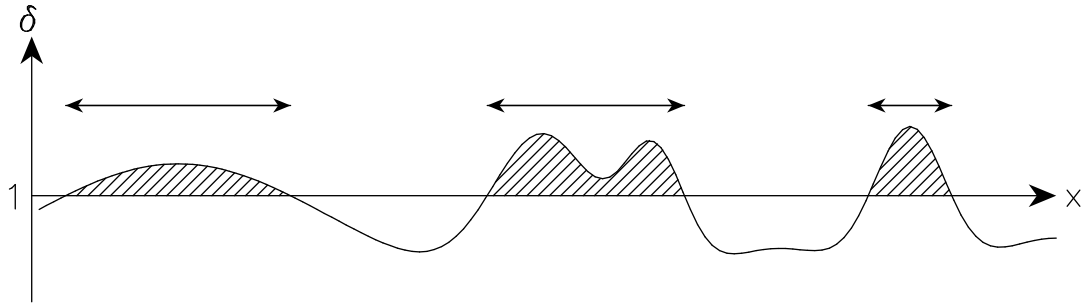


Fig. 11. Schematic identification method of clumps of WHIM.

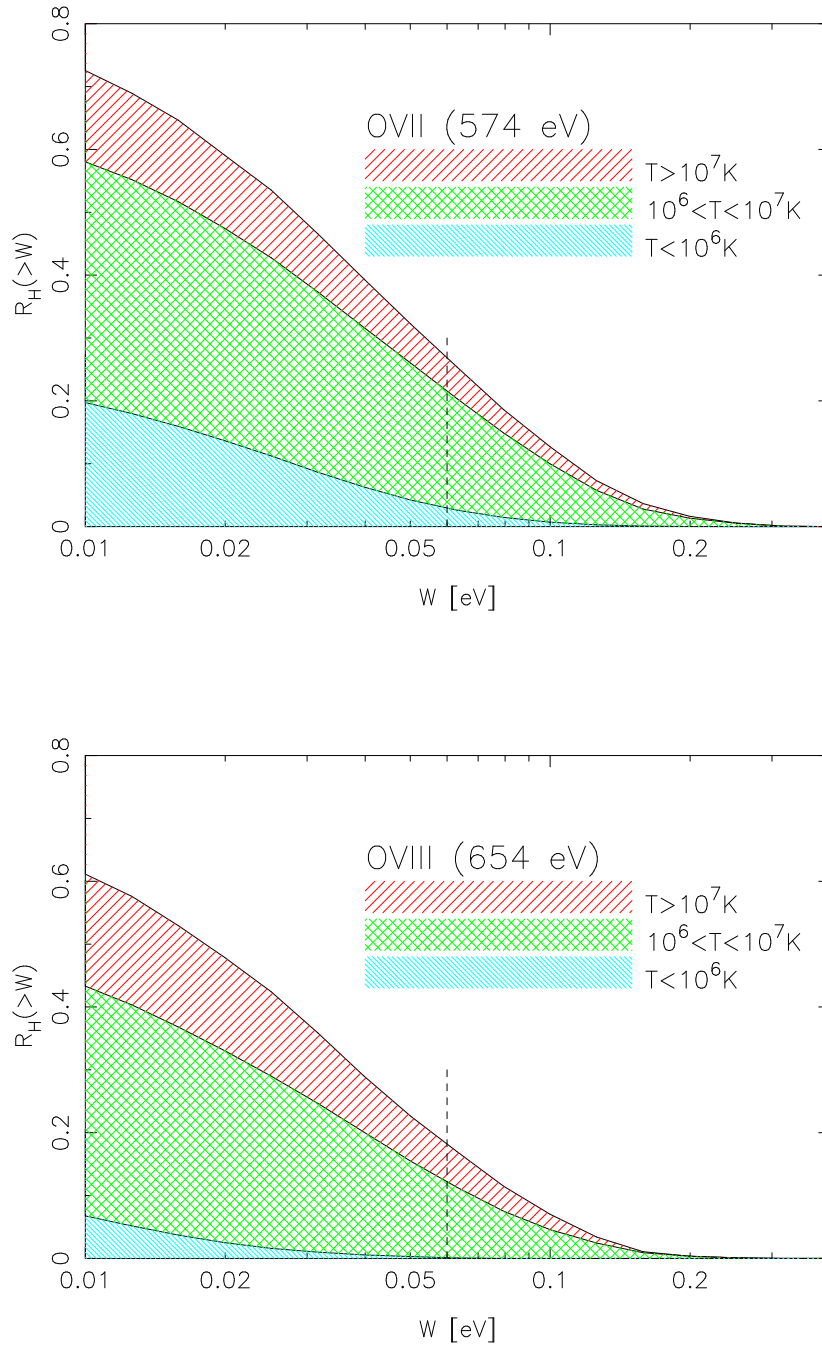


Fig. 12. Cumulative ratio of hydrogen column densities (eq.(27)) as a function of the equivalent width of the detected absorption line systems; OVII 574 eV (*upper panel*) and O VIII 654 eV (*lower panel*). The three shaded regions indicate the different temperature ranges; $T > 10^7$ K, $10^6 < T < 10^7$ K, $T < 10^5$ from top to bottom.

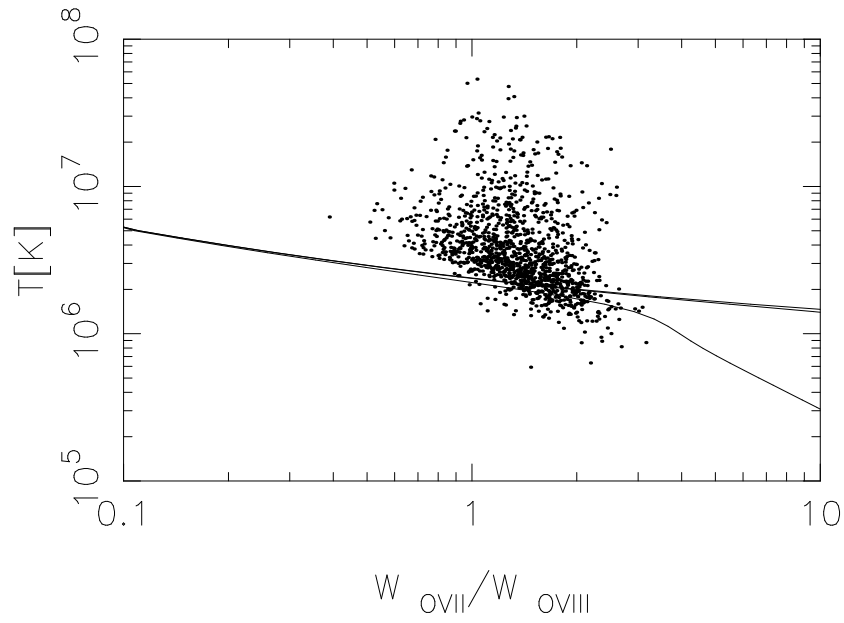


Fig. 13. The ratio of the O VII (574 eV) and O VIII (654 eV) equivalent width and the mass-weighted average temperature. The solid curves show the theoretical curves in the uniform case under CPlE assuming the hydrogen number density $n_H = 10^{-5}, 10^{-6}, 10^{-7} \text{ cm}^{-3}$ from top to bottom.

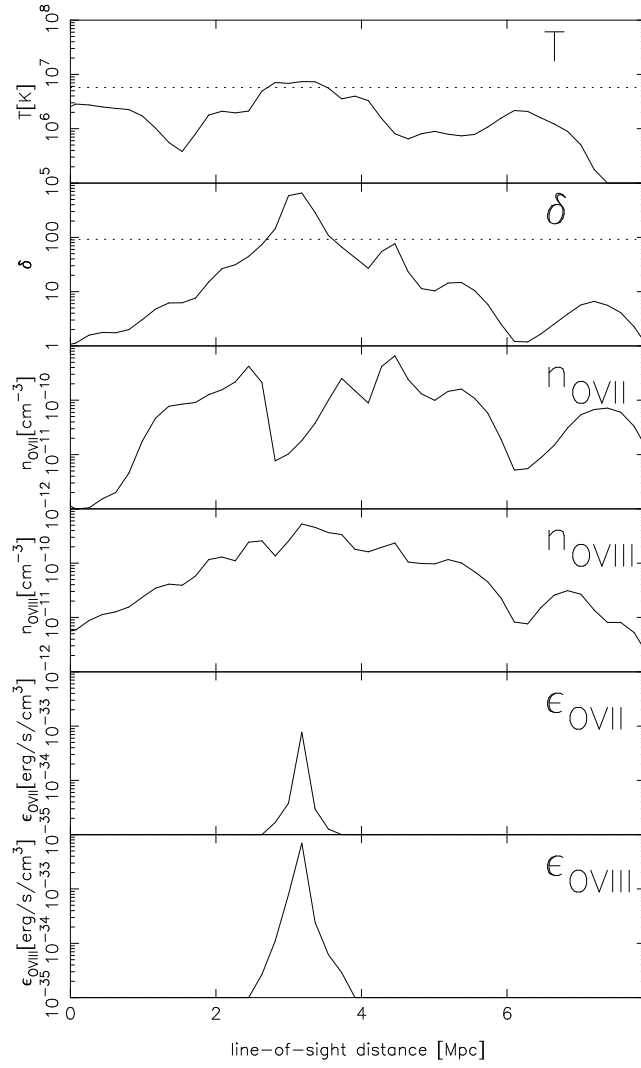


Fig. 14. An example of sub-structure in a WHIM which forms a single absorption line system. From top to bottom, we show temperature, over-density, number density of O VII, number density of O VIII, emissivity of OVII, emissivity of O VIII.

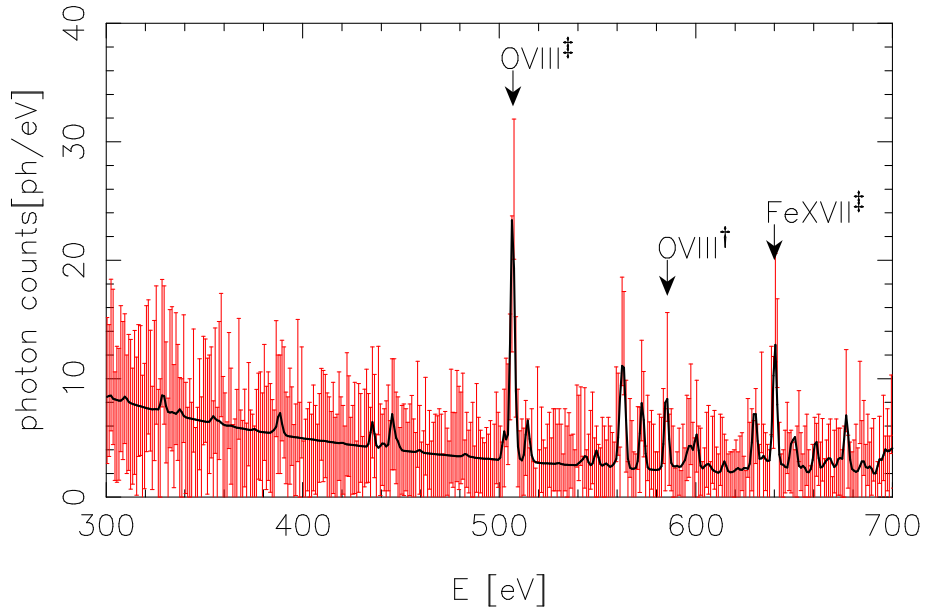


Fig. 15. The emission spectrum toward the LOS A after the CXB emission is subtracted. We assume 1 pixel size ($1/256 \text{ deg}^2$) and the exposure time $T_{\text{exp}} = 10^6 \text{ s}$ for *DIOS*. The error bars indicate 1σ of Poisson noise which includes WHIM emission and CXB.

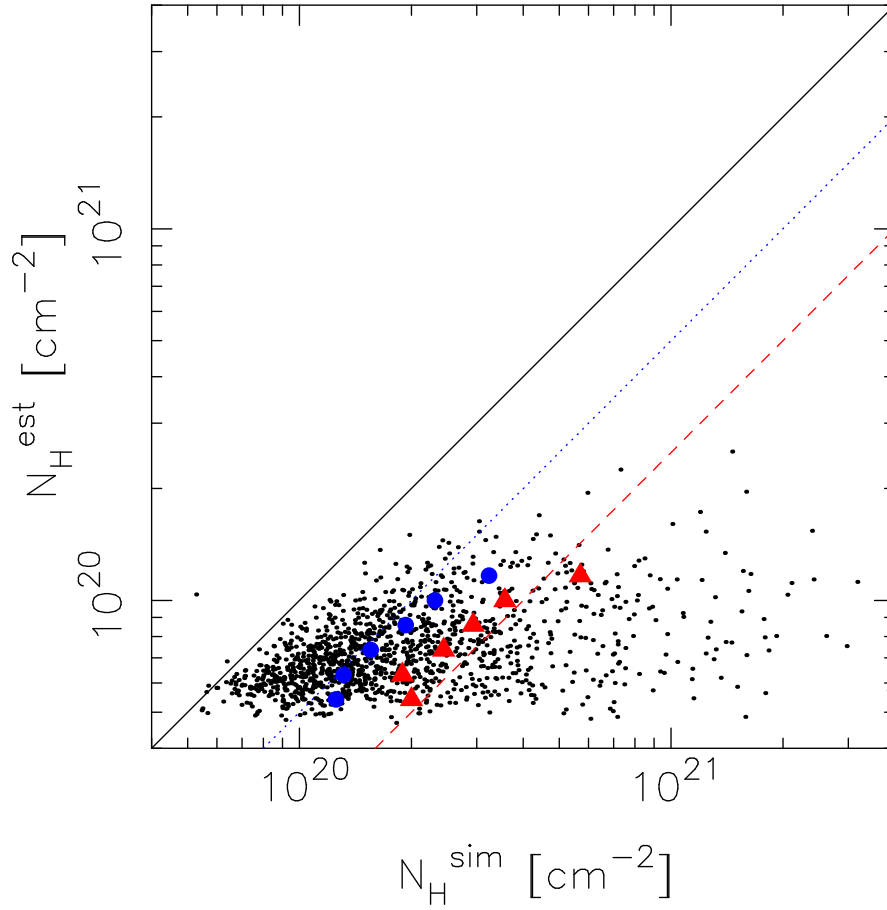


Fig. 16. Comparison between $N_H^{\text{est}}(> 3\sigma)$ and $N_H^{\text{sim}}(> 3\sigma)$. Each dot represent a WHIM clump which exhibit both OVII and OVIII with $S/N > 3$ (1315 clumps in total). The filled circles and triangles indicate the mean and median values of $N_H^{\text{sim}}(> 3\sigma)$ for the fixed bin with respect to $N_H^{\text{est}}(> 3\sigma)$. The solid, dotted and dashed lines show $N_H^{\text{est}}(> 3\sigma)/N_H^{\text{sim}}(> 3\sigma) = 1, 1/2,$ and $1/4,$ respectively.

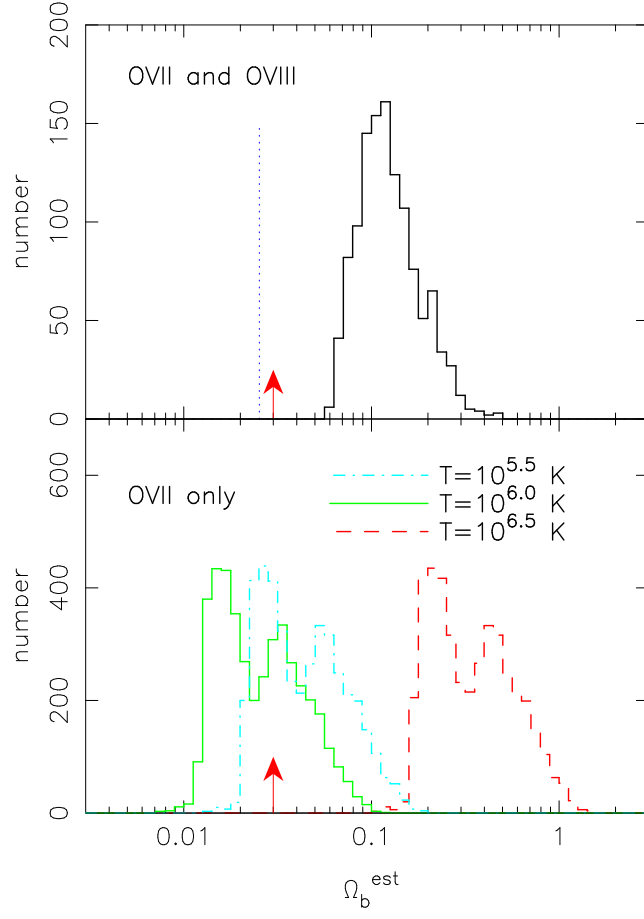


Fig. 17. Histogram of Ω_b^{est} estimated according to eq.(34). The Upper panel shows the case that both OVII and OVIII are detected and temperature is estimated from their line ratio. The vertical dotted line is the mean value 0.025 computed from the entire LOSs including non-detection. The lower panel shows an estimation using only O VII absorption lines assuming temperature $T = 10^{5.5}$, $10^{6.0}$, and $10^{6.5}$ K. The arrow indicates the value of $\Omega_b (= 0.03)$ that is adopted in our numerical simulation.